Controller Strategy for Open-Winding Brushless Doubly-Fed Wind Power Generator with Common Mode Voltage Elimination

Fengge Zhang, *Member, IEEE*, Liancheng Zhu, Shi Jin, *Member, IEEE*, Xiaoying Su, Sul Ademi, *Member, IEEE*, and Wenping Cao, *Senior Member, IEEE*

***Abstract*—This paper presents the theoretical derivation and implementation of a novel direct power control for open-winding brushless doubly-fed reluctance generator (OW-BDFRG). As one of the promising brushless candidates, the OW-BDFRG is characterized with two stator windings fed by a dual controllable two-level three-phase converters through a common DC bus with common mode voltage elimination. The parameter-free control strategy is designed to obtain maximum power point tracking with variable speed constant frequency (VSCF) for wind energy conversion systems (WECSs). Compared to the traditional three-level converter systems, the DC bus voltage, AC-side voltage and capacity ratings of the proposed converter system are notably high while the reliability, redundancy and fault tolerance are significantly improved. Effectiveness, correctness and robustness of the proposed control strategy and the common mode voltage elimination scheme are evaluated and confirmed through simulation and experimental tests on a 42 kW generator prototype typical for VSCF-WECS.**

***Index Terms*—Brushless doubly-fed machines, power control, common mode voltage, open-winding, variable speed constant frequency, maximum power point tracking.**

NOMENCLATURE

u_p, u_c	Power, control winding phase voltages [V]
i_p, i_c	Power, control winding phase currents [A]
R_p, R_c	Power, control winding resistances [Ω]
p_p, p_c, p_r	Power, control and rotor pole pairs
L_p, L_c	Power, control winding self-inductan. [H]
ψ_p, ψ_c	Power, control winding flux linkages [Wb]
ψ_{pc}, L_{pc}	Mutual flux [Wb] and inductance [H]
$f_p, f_c, \omega_p, \omega_c$	Power, control winding frequencies [Hz] and their angular frequencies [rad/s]
n_r, ω_{rm}	Rotor speed [r/min] and angular velocity [rad/s]
T_{em}	Electromagnetic torque [N·m]
σ	Leakage factor $= 1 - L_{pc}^2/(L_pL_c)$
D	Differential operator = d/dt
P_m, P_{pm}, P_{cm}	Mechanical (shaft) power and its power control components [W]
P_p, Q_p	Real power [W] and reactive power [VAr]
P_{pem}, P_{cem}	Power, control-winding electromagnetic power [W]
p_{pFe}, p_{pCu}	Power winding core and copper losses [W]
p_{rFe}, p_m, p_{ad}	Rotor core, mech. and additional losses

Manuscript received October 22, 2017; revised January 26, 2018; accepted February 10, 2018. This work was supported in part by the National Natural Science Foundation of China under Grant 51537007, and the Natural Science Foundation of Liaoning Province, China, under Grant 201602540 and Youth Foundation of University of Science and Technology Liaoning, China, under Grant 2012QN29.

F. Zang, L. Zhu, S. Jin and X. Su are with the School of Electrical Engineering, Shenyang University of Technology, Shenyang, P. R. China. L. Zhu and X. Su are also with the School of Electronic and Information Engineering, University of Science and Technology Liaoning, Anshan, P. R. China. (e-mail: zhangfg@sut.edu.cn; zhuliancheng@163.com; wby-js@163.com; misky88@sina.com). (Corresponding author: L. Zhu: 0086-412-5929711; fax: 0086-412-5929129; e-mail: zhuliancheng@163.com)

S. Ademi is with the Warwick Manufacturing Group (WMG), University of Warwick, Coventry, U.K. (e-mail: s.ademi@warwick.ac.uk)

W. Cao is with the School of Engineering and Applied Science, Aston University, Birmingham, U.K. (e-mail: w.p.cao@aston.ac.uk).

I. INTRODUCTION

BRUSHLESS doubly-fed generators (BDFGs) [1]–[3] have been regarded as forthcoming alternatives of the slip-ring doubly-fed induction generator (DFIG) for variable speed constant frequency (VSCF) with limited speed applications [3]. The recent advancement in the field indicates that BDFGs entail comparable performance advantages to DFIG in terms of economic benefits of reduced converter rating, inherently decoupled control of power winding torque (active) and reactive power for a typical speed range of 2:1 in wind energy conversion systems (WECS) [4], [5]. Another distinct advantage of BDFGs is the flexible modes of operation [6], [7], making them suitable for maximum power point tracking (MPPT) for VSCF-WECS [1], [3]. Due to the increasing development of new energy distributed generation, grid demands for new and challenging requirements imposing WECS to provide reactive and active power to help stabilize the power system under some disturbances [8].

Giving recognition to the BDFGs relatively higher leakage inductances and thus lower transient fault current in low-voltage ride-through without the need of supplementary crowbar circuitry makes BDFGs seemingly superior to the DFIG for grid-connected power generation [9]. Comparing the drawbacks of reliability and maintenance of DFIG for long-term use in medium or large-scale applications, the brushes and slip-rings have been removed in BDFGs design by moving the DFIG controllable rotor winding to the stator as the control winding to obtain higher robustness and maintenance-free operation [10], [11]. Except for the above features, due to the absence of rotor winding, open-winding brushless doubly-fed reluctance generator (OW-BDFRG) has further merits in

This article has been accepted for publication in a future issue of this journal, but has not been fully edited. Content may change prior to final publication. Citation information: DOI 10.1109/TIE.2018.2811370, IEEE Transactions on Industrial Electronics

terms of competitive efficiency [10] and simpler dynamic model, thus easier to implement control [2], [6]. The OW-BDFRG consists of two distributed stator windings of normally different applied frequencies and pole numbers, with a cageless reluctance rotor having half the total number of two stator poles to provide the shaft position dependent indirectly coupling between windings and torque production [3]. The power (primary = p_p, f_p) winding is grid-connected while the open-circuited control (secondary = p_c, f_c) winding is supplied through a dual two-level converter via the DC-link in Fig. 1.

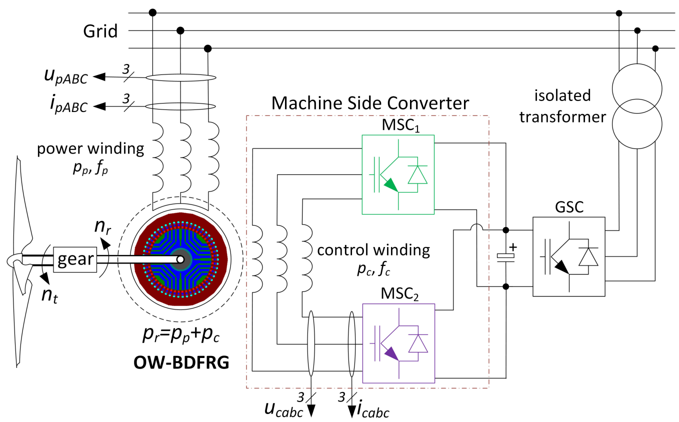

Fig. 1. A simplified schematic of the OW-BDFRG wind turbine system.

The control schemes investigated and validated for the BDFRG include voltage oriented control [12], field oriented control with [13], [14] or without [15] an encoder position sensor, torque control with [15], [16] and without [17] a speed sensor for speed regulation under different loading profiles. The direct power control (DPC) inferred from direct torque control (DTC) scheme [15], has the advantage of parameter-freedom, more robust and simpler power controllability.

Although the DPC is achieved by controlling the converter control winding, the flux sectorial location of control winding need to be identified from the measurable power winding of the reactive power but not the exact flux position information [18]. Considering the rated capacity limits of the two-level [19], inherent disadvantages of three-level systems [19], [20], improvised performance of four-level strategies [21] in terms of complex topology, high voltage of the DC bus and the potential drift of neutral point [22], makes them all difficult to implement in the megawatt applications. To improve the aforementioned challenges and shortcomings of such converters for the megawatt in VSCF-WECS, the correctness and effectiveness of the proposed control strategy for the promising OW-BDFRG are investigated through simulation and experimental tests. Consequently, the design methodology and its feasibility are evaluated, while the main contributions of the paper are brought to focus.

1) A parameter-free direct power control strategy combined with maximum power point tracking are investigated to examine the efficacy of the controller performance, accuracy and robustness.
2) Dual two-level four-quadrant machine side converter (MSC_1 and MSC_2) arrangement using a common DC bus through a single grid side converter (GSC) is configured to drive the emerging OW-BDFRG.
3) An optimized pulse width modulation switching scheme with common mode voltage elimination is proposed, investigated and applied to the OW-BDFRG controller design.

Compared to the three-level converter systems, the reliability, redundancy and fault tolerance of the proposed OW-BDFRG system is greatly improved. Subsequently, the DC-link voltage and the rated capacity of power devices on the MSC_1 and MSC_2 are reduced by about 50%, while keeping the complexity of the main circuit topology the same in contrast to the two-level converter structure.

This paper is organized as follows. The mathematical model, operating principles and variable speed constant frequency aligned with maximum power point tracking configuration are constructed in Section II. Dual two-level converter (MSC_1 and MSC_2) driving the OW-BDFRG, a combination of direct power control mechanism, common mode voltage elimination and effects of voltage vector on power variations are developed and outlined in Section III. Simulation and experimental results verify the accuracy and robustness of the control strategy in Section IV. Finally, Section V draws conclusion.

II. OW-BDFRG Modeling and Operating Principles

A. Dynamic Modeling

The space-vector model of the power and control windings in arbitrary rotating $d-q$ frame employing *generating* convention can be represented as (1) and (2) [6].

$$\begin{cases} u_{pq} = -R_p i_{pq} - DL_p i_{pq} + DL_{pc} i_{cq} + \omega\psi_{pd} \\ u_{pd} = -R_p i_{pd} - DL_p i_{pd} + DL_{pc} i_{cd} + \omega\psi_{pq} \\ u_{cq} = R_c i_{cq} + DL_c i_{cq} - DL_{pc} i_{pq} - (\omega-\omega)\psi_{cd} \\ u_{cd} = R_c i_{cd} + DL_c i_{cd} + DL_{pc} i_{pd} - (\omega-\omega)\psi_{cq} \end{cases} \tag{1}$$

where, 'D' represents the differential operator (d/dt), subscripts 'p' and 'c' denote corresponding stators and 'r' represents rotor components; ω, $\omega-\omega_r$ and ω_r indicates the rotating speed of d_p-q_p, d_c-q_c frames and the rotor angular.

$$\begin{cases} \psi_{pq} = L_p i_{pq} - L_{pc} i_{cq} \\ \psi_{pd} = L_p i_{pd} + L_{pc} i_{cd} \\ \psi_{cq} = L_c i_{cq} - L_{pc} i_{pq} \\ \psi_{cd} = L_c i_{cd} + L_{pc} i_{pd} \end{cases} \tag{2}$$

where, $\omega=\omega_p$, $\omega_r-\omega_p=\omega_c$, thus the power and control winding expressions refer to different reference frames rotating at ω_p and ω_c as depicted in Fig. 2.

B. Principle operation of OW-BDFRG with VSCF-MPPT

The magnetic barrier reluctance rotor affords such a magnetic coupling between stator windings by modulating their magneto-motive forces in a frequency conversion based on the angular velocity relationship and its unusual electromagnetic torque production:

$$f_p = \frac{n_r(p_p+p_c)}{60} \pm f_c \tag{3}$$

$$\omega_{rm} = \frac{2\pi n_r}{60} = \frac{\omega_p+\omega_c}{p_r} = \omega_{syn}(1+\frac{\omega_c}{\omega_p}) \tag{4}$$

This article has been accepted for publication in a future issue of this journal, but has not been fully edited. Content may change prior to final publication. Citation information: DOI 10.1109/TIE.2018.2811370, IEEE Transactions on Industrial Electronics

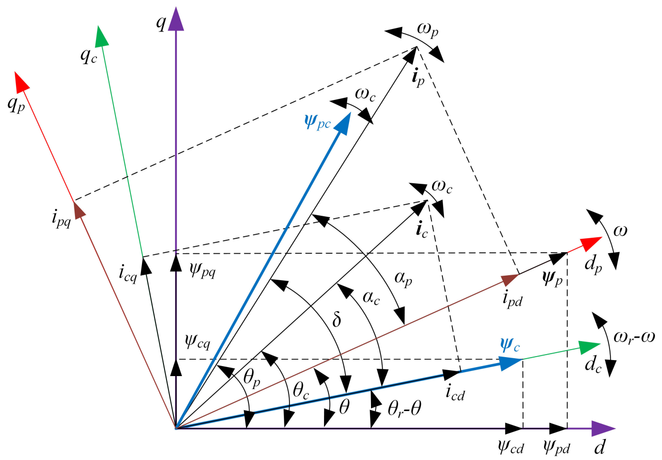

Fig. 2. Characteristic space vectors and reference frame alignment.

$$T_{em} = \frac{3p_r}{2\sigma L_c}|\boldsymbol{\psi}_{pc} \times \boldsymbol{\psi}_c| = \frac{3p_r}{2\sigma L_c}|\boldsymbol{\psi}_{pc}||\boldsymbol{\psi}_c|\sin\delta \quad (5)$$

where, $\omega_{syn} = \omega_p/p_r$ for $\omega_c = 0$ (DC control winding) represents the synchronous speed, $\sigma = 1 - L_{pc}^2/(L_p L_c)$ indicates the leakage factor, $\Psi_{pc} = \Psi_p(L_{pc}/L_p)$ denotes the mutual flux linkage between the two stator windings. Note that if $\omega_{rm} > \omega_{syn}$, (3) gets '-' for super-synchronous and $\omega_c > 0$, the phase sequence of control winding is the same as the power winding; if $\omega_{rm} < \omega_{syn}$, (3) takes '+' for sub-synchronous, and $\omega_c < 0$, where the phase sequence is opposite in the stator windings. Using (4), the mechanical power balance shows individual contributions of each winding considering angular velocity and pole arrangements can be represented as [11]:

$$P_m = T_{em}\omega_{rm} = \underbrace{T_{em}\cdot\frac{\omega_p}{p_r}}_{P_{pm}\approx P_p} + \underbrace{T_{em}\cdot\frac{\omega_c}{p_r}}_{P_{cm}\approx P_c} = \underbrace{P_{pm}}_{\approx P_p}(1-s) \quad (6)$$

where, $P_{cm}(P_c) < 0$ (producing power to the grid) for super-synchronous and $P_{cm}(P_c) > 0$ (absorbs power from the grid) for 'sub-synchronous' mode. The power flow chart implying to (6) is presented in Fig. 3. Note that only $P_{pm} < 0$ (i.e., $P_p < 0$) component is investigated in this paper for VSCF-WECS.

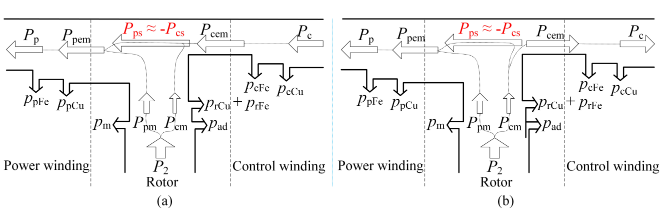

Fig. 3. Power flow chart of the OW-BDFRG for generator operation. (a) Sub-synchronous mode. (b) Super-synchronous mode ($n_r < n_p$).

By adjusting f_c and its phase sequence along with n_r can maintain constant line frequency f_p and make OW-BDFRG suitable candidate in VSCF applications such as wind turbines, ship shaft power generation and hydroelectric generators. Moreover, expression (5) is not used for control purpose but only helping to illustrate the controller principles as further detailed in the Section III. C.

C. Maximum Power Point Tracking of the OW-BDFRG

The mechanical power captured by the wind turbine can be expressed as (7), which meets expression (8) [8]:

$$P_m = \frac{1}{2}C_p\rho\pi R^2 v_w^3 \quad (7)$$

$$C_p(\lambda,\beta) = 0.5176(\frac{116}{\lambda_i} - 0.4\beta - 5)e^{-\frac{21}{\lambda_i}} + 0.0068\lambda \quad (8)$$

where, P_m (kW), β (°), λ, C_p, v_w (m/s) and n_r (r/min), denoting the mechanical power of the wind turbine, pitch angle, tip speed ratio, wind power utilization coefficient, wind speed and the rotor speed of OW-BDFRG, respectively. The wind turbine parameters are deduced as the start-up, rated and intermittent range of wind speeds as 3 m/s, 12 m/s and 3–25 m/s. While the wind wheel diameter considered is 11.85 m and air density being 1.225 kg/m^3. The rated power is 50 kW, with the gear ratio of 5.2, consequently the performance curves of the wind turbine is presented in Fig. 4. It is worth noting that β should be minimized in order to make the best of wind energy captured by the turbine as indicated in Fig. 4(a), when v_w is below its rating value, one can set $\beta = 0$ for capturing the maximum power coefficient C_p = 0.48. Furthermore, the rotor speed is adjusted according to each maximum power tracking point as illustrated in Fig. 4(b).

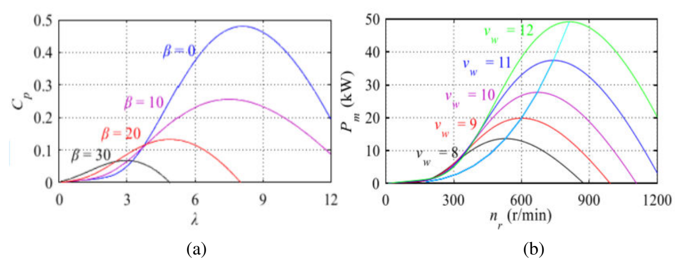

Fig. 4. Performance curves of the wind turbine. (a) C_p- λ curves at different β and (b) P_m-n_r curves and their MPPT at different speeds.

III. DPC Strategy with Common Mode Voltage Elimination for OW-BDFRG

A. Dual Two-level Converter Structure

The control phase windings are open-circuited fed by the dual two-level converters using a common DC bus (Fig. 1). Consequently, the topology can be described in two-fold: upper bridge arm (MSC_1) configured as 1 to 6 and lower bridge arm (MSC_2) allocated as $1'$ to $6'$ as illustrated in Fig. 5, whereby comparing OW-BDFRG with the OW-PMSG(M) [23], [24] and OW-IM (induction motor) [21], [25], one can obtain overwhelming virtues in terms of its partially-rated capacity and four-quadrant power. Advantages of the multi-phase machines over the traditional three-phase machines, such as capabilities in starting and continue running even with one or more of stator phases open-circuited or short-circuited, reduction in the torque pulsation and rotor copper loss hence result in improving overall performance and increasing power rating without enhancing every phase voltage, which make they be suitable for naval vessel propulsion systems and so on. However, the multi-phase machines still face many important technical challenges which need to be overcome as comprehensively addressed in [26]. In this paper, the proposed open-winding BDFRG fed with dual two-level converters can also improve the reliability, redundance, reduce the rating in single converter but can increase the output level, which makes OW-BDFRG easier to implement in VSCF and MPPT by only adjusting the f_c amplitude and its phase sequence along with different rotor speed (sub-synchronous, synchronous or super-synchronous mode).

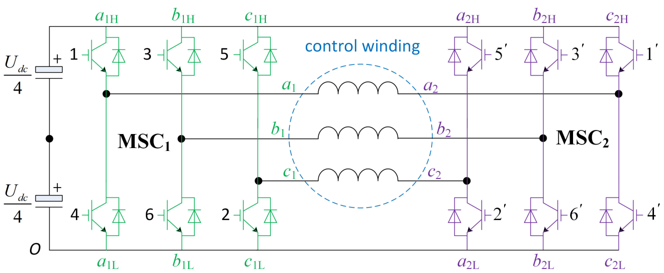

Fig. 5. Configuration of OW-BDFRG with dual two-level converters.

Therefore, the voltage relationships are denoted as:

$$\begin{cases} u_{ca} = u_{a_1o} - u_{a_2o} = u_{a_1a_2} \\ u_{cb} = u_{b_1o} - u_{b_2o} = u_{b_1b_2} \\ u_{cc} = u_{c_1o} - u_{c_2o} = u_{c_1c_2} \end{cases} \tag{9}$$

The voltage (also current and flux) in the control winding can be controlled by applying the coordinated voltage space vectors via selecting the suitable switching mode in MSC_1 and MSC_2, for the combination $15'$. One can also select the MSC_1 and MSC_2 as '100' and '001' mode, respectively as shown Fig. 6(a), thus leads to $u_{ca} = u_{dc}/2$, $u_{cb} = 0$ and $u_{cc} = -u_{dc}/2$.

B. Combinations and Optimization Methods of the Voltage Space Vectors

For the traditional two-level converter topology (MSC_1 and MSC_2), their voltage vectors can be expanded and described with the space span divided into six corresponding sectors as shown in Fig. 6(a), where the switching mode is $2^3 = 8$, and the effective and zero vectors are represented as 1–6, $1' - 6'$ and 7, 8, $7', 8'$. The combinations of the voltage space vectors in Fig. 5 are embodied in Fig. 6(b) by synthesizing the former with the switching modes increasing to $2^3 \times 2^3 = 64$ (vectors illustrated as $11'$–$88'$), and the space span dividing into 24 sectors obtaining identical voltage vectors (OA, OB, $\cdots$, OS) which is the same as Fig. 7 in the conventional three-level converter [19]. However, unlike $3^3 = 27$ switching modes in Fig. 7, the redundancy and fault tolerance of the proposed topology are much higher ($64 > 27$). By comparing Fig. 6(b) with Fig. 7, the numbers of long vectors are all equal to 6 (OG, OI, OK, OM, OP, OR), the medium vectors are twice to the latter (12 vs 6, OH, OJ, OL, ON, OQ, OS), while the short vectors are three times to the latter (36 vs 12, OA, OB, OC, OD, OE, OF), and the zero vectors (O) add up to 10 from 3. Note that the DC-link voltage in the proposed topology (Fig. 5) is only 50% ($U_{dc}/2$) of the traditional three-level-converter fed systems (U_{dc}) [19].

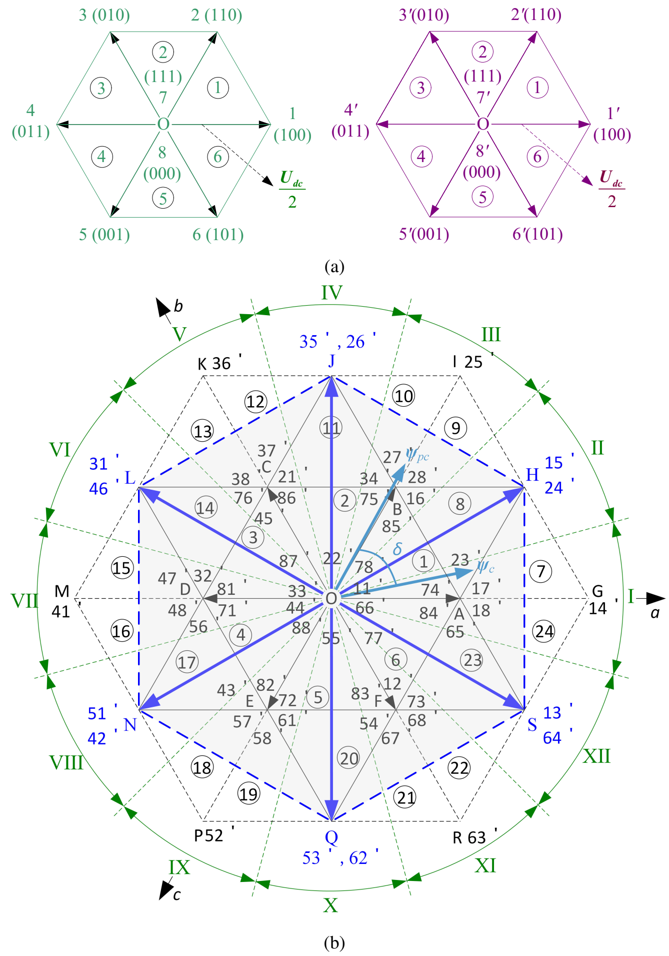

Fig. 6. Voltage space vectors characteristic. (a) Vectors in MSC_1 and MSC_2 and (b) Vectors, 60° sectors and effects on power variations of the specified vector combinations with CMV = 0 in dual two-level converters.

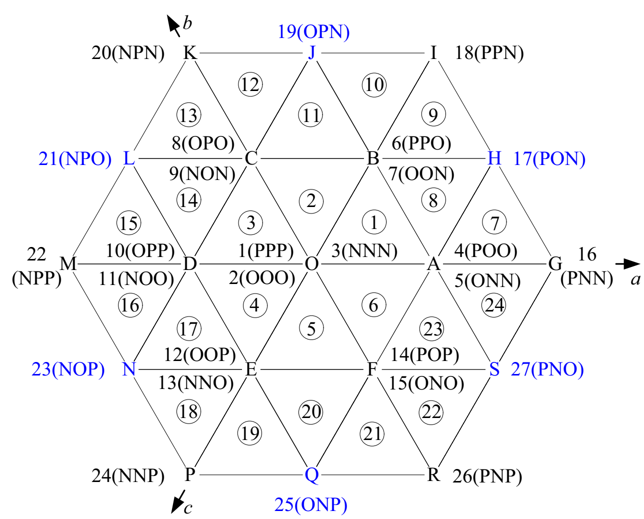

Fig. 7. The voltage space vector and sector representation of the traditional three-level converter.

When using a common DC bus, the common mode voltage of the control winding in Fig. 5 can be represented as:

$$\begin{cases} u_{\mathrm{CMV}_1} = (u_{a_1o} + u_{b_1o} + u_{c_1o})/3 \\ u_{\mathrm{CMV}_2} = (u_{a_2o} + u_{b_2o} + u_{c_2o})/3 \\ \quad u_{\mathrm{CMV}} = u_{\mathrm{CMV}_1} - u_{\mathrm{CMV}_2} \end{cases} \tag{10}$$

For the vector $15'$, the CMV is 0 as expressed in (11), hence other vectors with CMV = 0 can be obtained as OH, OJ, OL, ON, OQ, OS and O, thus the effective vectors are only the middle ones. To implement the proposed direct power control strategy, the voltage space vectors with CMV elimination are shown in Fig. 6(b), divided into 12 sectors (I-XII).

$$\begin{aligned} u_{\mathrm{CMV}} &= u_{\mathrm{CMV}_1(100)} - u_{\mathrm{CMV}_2(001)} \\ &= (U_{dc}/2 + 0 + 0) - (0 + 0 + U_{dc}/2) = 0 \end{aligned} \tag{11}$$

C. DPC Mechanisms and Controller Strategy

The proposed direct power control schematic diagram is presented in Fig. 8, where P_{pref} denotes the optimum performance indicators by considering MPPT in VSCF-WECS, while Q_{pref} is dedicated to regulate and achieve unity power factor control.

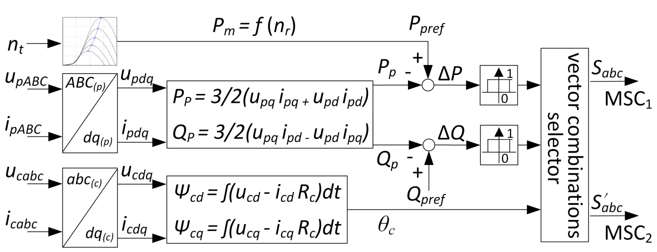

Fig. 8. A structural diagram of the proposed DPC strategy for OW-BDFRG wind turbine with maximum power point tracking controller.

Furthermore, by employing (12), the instantaneous primary electrical real and reactive power in the power winding can be expressed as:

$$\begin{cases} P_p = 3/2(u_{pq}i_{pq} + u_{pd}i_{pd}) \\ Q_p = 3/2(u_{pq}i_{pd} - u_{pd}i_{pq}) \end{cases} \tag{12}$$

To explicate the direct power control mechanism one can neglect the copper losses in view of the larger machines having inherently lower resistances [18] and also ignoring the variation of energy stored in the magnetic field (dW/dt) with a view to the $\Psi_p \approx$ constant (also $\Psi_{pc} \approx$ constant) since the power winding is grid-connected, $dW/dt \approx d\Psi_p/dt \approx 0$. Thus, the active power is almost equal to its mechanical power, $P_p \approx P_{pm}$ (also, $P_c \approx P_{cm}$) according to (6). Referring to the DTC approach in [15], [16] and providing the power and control winding flux in (13) and (14), then the mechanisms of the proposed DPC can be interpreted (but not for control) as: P_p is controllable by adjusting the $\boldsymbol{\psi}_c$ angle ($\theta_r - \theta = \theta_c$), if $|P_p|$ is expected to increase/decrease (generating more/less power to the grid). One can increase/reduce δ according to electromagnetic torque (T_{em}) expression in (5) and mechanical power balance contribution to individual winding in (6) as reinstated in Fig. 3.

$$\begin{cases} \boldsymbol{\psi}_p = \int(\boldsymbol{u}_p - R_p\boldsymbol{i}_p)dt \\ \boldsymbol{\psi}_c = \int(\boldsymbol{u}_c - R_c\boldsymbol{i}_c)dt \end{cases} \tag{13}$$

$$\begin{cases} \psi_{cd} = \int(u_{cd} - R_c i_{cd})dt \\ \psi_{cq} = \int(u_{cq} - R_c i_{cq})dt \end{cases} \tag{14}$$

The Q_p control can be explicated with similar notion to P_p, however, different in logic due to the doubly-excited principles. Since power and control windings jointly participate in establishing the machine flux, one winding participates more/less flux, while the other winding contributes less/more in the process of excitation and flux build-up. Moreover, the changes of Ψ_p are closely related to that of the reactive power, thus, the increasing/decreasing Q_p can be attained by increasing/decreasing the magnetizing current (Ψ_p) from the power winding. Such an intricate procedure can be achieved by decreasing/increasing the corresponding related control winding component (Ψ_c), from the controllable optimal combinations of the output vectors on MSC_1 and MSC_2.

D. Effects of Voltage Vectors on Power Variations

In order to fulfil the proposed direct power control strategy using the optimized voltage space vectors for MSC_1 and MSC_2 through a common DC bus with CMV elimination the optimized voltage vectors selected $15'$, $35'$, $31'$, $51'$, $53'$, $13'$, $24'$, $26'$, $46'$, $42'$, $62'$, $64'$ are displayed in Fig. 6(b) with shaded hexagon area as HJLNQS. The $\boldsymbol{\psi}_c$ and active power dynamics are reliant on the flux instant position, whereby assuming that $\boldsymbol{\psi}_c$ is located in sector I and lag $\boldsymbol{\psi}_{pc}$ with δ at a given time instant as shown in Fig. 6(b).

In generating mode, $P_p < 0$, the OW-BDFRG absorbs mechanical power ($P_{pm} < 0$) from the rotor and produces positive P_p to the grid by the power winding generated by the wind turbine (Fig. 3). Employing voltage vectors OH or OL moves $\boldsymbol{\psi}_c$ rotation anti-clockwise, resulting in the decrease with angle δ and increase with P_p refers to (5), the P_p becoming less negative, which indicates the OW-BDFRG would produce less real power to the grid. On the other hand if vectors ON or OS were chosen subsequently the $\boldsymbol{\psi}_c$ moves clockwise with increasing δ and reducing P_p (more negative), which would produce more real power to the grid. Irrespective of whether the BDFMs operate as a motor or a generator the effects of voltage space vectors on the real powers have the same result. If $\boldsymbol{\psi}_c$ is located in the k^{th} (k = I, II, $\cdots$, XII) sector, then the vector combinations in $(k^{th}+1)$ or $(k^{th}+2)$ increases the P_p and the vectors in $(k^{th}-1)$ or $(k^{th}-2)$ decreases the P_p (Fig. 6(b)).

According to subsection C, using any vectors of OH or OS increases Ψ_c and Ψ_{cd} (Fig. 2), indicating that there will be more reactive power to be supplied by the converters, hence the Q_p will be reduced. Inversely, vectors OL or ON will reduce Ψ_c, Ψ_{cd} and Q_c, consequently, the Q_p will be increased. Similarly to the P_p control summary, the Q_p control rules can be concluded as follows, if the $\boldsymbol{\psi}_c$ lies in the k^{th} sector, then the vector combinations in $(k^{th}-1)$, k^{th} or $(k^{th}+1)$ reduces and vectors in $(k^{th}+2)$, $(k^{th}+3)$ or $(k^{th}-2)$ will increase Q_p (Fig. 6(b)). The voltage vector effects on real and reactive power variations of the power winding in each sectors are tabulated in Table I, where $dP_p > 0$, $dQ_p > 0$ (or < 0) denoting that the P_p and Q_p will be increased (or reduced), respectively.

This article has been accepted for publication in a future issue of this journal, but has not been fully edited. Content may change prior to final publication. Citation information: DOI 10.1109/TIE.2018.2811370, IEEE Transactions on Industrial Electronics

TABLE I
VECTOR EFFECTS ON POWER VARIATIONS

Sector\Change	$dP_p > 0$	$dP_p < 0$	$dQ_p > 0$	$dQ_p < 0$
I	OH, OL	ON, OS	OL, ON	OH, OS
II	OJ, OL	OQ, OS	OL, OQ	OJ, OS
III	OJ, ON	OH, OQ	ON, OQ	OH, OJ
IV	OL, ON	OH, OS	ON, OS	OH, OL
V	OL, OQ	OJ, OS	OQ, OS	OJ, OL
VI	ON, OQ	OH, OJ	OH, OQ	OJ, ON
VII	ON, OS	OH, OL	OH, OS	OL, ON
VIII	OQ, OS	OJ, OL	OJ, OS	OL, OQ
IX	OH, OQ	OJ, ON	OH, OJ	ON, OQ
X	OH, OS	OL, ON	OH, OL	ON, OS
XI	OJ, OS	OL, OQ	OJ, OL	OQ, OS
XII	OH, OJ	ON, OQ	OJ, ON	OH, OQ

TABLE II
EXPECTED ΔQ $(+/-)$ AND SECTOR INCREMENTS $(+1/-1)$

Sec.\Vec.	OH	OJ	OL	ON	OQ	OS
I	$-\|-1$	x	$+\|+1$	$+\|-1$	x	$-\|+1$
II	x	$-\|+1$	$+\|-1$	x	$+\|+1$	$-\|-1$
III	$-\|+1$	$-\|-1$	x	$+\|+1$	$+\|-1$	x
IV	$-\|-1$	x	$-\|+1$	$+\|-1$	x	$+\|+1$
V	x	$-\|+1$	$-\|-1$	x	$+\|+1$	$+\|-1$
VI	$+\|+1$	$-\|-1$	x	$-\|+1$	$+\|-1$	x
VII	$+\|-1$	x	$-\|+1$	$-\|-1$	x	$+\|+1$
VIII	x	$+\|+1$	$-\|-1$	x	$-\|+1$	$+\|-1$
IX	$+\|+1$	$+\|-1$	x	$-\|+1$	$-\|-1$	x
X	$+\|-1$	x	$+\|+1$	$-\|-1$	x	$-\|+1$
XI	x	$+\|+1$	$+\|-1$	x	$-\|+1$	$-\|-1$
XII	$-\|+1$	$+\|-1$	x	$+\|+1$	$-\|-1$	x

Analyzing Fig. 6(b) and Table I, one can attain the relation between the expected rate of change of Q_p and inferred direction of the control winding flux sector as shown in Table II, where '+' or '-' shows Q_p need to be increased/decreased ($Q_{pref} - Q_p > \Delta Q_p$, $dQ_p = 1$, or $Q_{pref} - Q_p < -\Delta Q_p$, $dQ_p = 0$, in Table III). The selected vector combinations in each sectors, 'x' indicates the abandoned combination(s) taking into account the opposite effect on Q_p, '+1' or '-1' represents increasing/reducing the sector number (k) (moving ψ_c anti-clockwise or clockwise) by using the specified vectors.

According to Table I, II and Fig. 6(b), one can deduce the post-optimized vectors for the DPC strategy shown in Table III. At any moment/sector, only one specialized vector combination is used to fulfil P_p and Q_p control requirements. In sector I, only vector OS can decrease both P_p and Q_p, and only OH can increase P_p and reduce Q_p. An important merit of the proposed OW-BDFRG for VSCF-WECS is that each of these vectors has two switching combination schemes (with hexagon HJLNQS), which is twice of the three-level converter systems shown in Fig. 7 [19]. Allowing for the same voltage space vectors of up/down row in Table III, only the up row switching combinations is adopted in this paper.

TABLE IV
PARAMETER SPECIFICATIONS AND RATINGS OF THE OW-BDFRG

Parameter	Value
Nominal power	42 kW
Nominal voltage	380 [V]
Pole-pairs number of power winding	3
Pole-pairs number of control winding	1
Resistance of power winding	0.1662 [Ω]
Resistance of control winding	0.1882 [Ω]
Self-inductance of power winding	17.37 mH
Self-inductance of control winding	23.51 mH
Mutual-inductance among the two stator windings	18.13 mH
Moment of inertia	0.3 kgm^2

IV. SIMULATION RESULTS AND EXPERIMENTAL VERIFICATION

A. Simulation Results

The 6/2-pole 42 kW OW-BDFRG prototype parameters obtained via off-line tests are shown in Table IV. To make the simulations accurate, the natural wind speed is simulated in a step signals superimposed fashion with high-frequency uncorrolated white noise and unknown DC offset in view of the voltage/current sensors errors. Setting ΔP_p to ± 0.6 kW, ΔQ_p to ± 0.4 kvar. The wind speed employed in this investigation are 8 m/s at the time interval of 0 s, then ramps up to 9 m/s and 10 m/s at 1.5 s and 3.5 s intervals, while the corresponding rotor speed values are changed in a ramp fashion with a 350 r/mins slope in order to simulate the real wind energy conversion system. The self-starting procedure has been neglected for ease of simplicity and also given the fact that the control action is not engaged after a certain time interval. The simulation results (Figs. 9–11) have been generated based on MATLAB/Simulink and SimPowerSystems toolbox, which have been successfully verified with the experimental measurements in Figs. 13–16. Given the test scenarios the discussion of the simulation and experimental results will be jointly discussed in the next subsection.

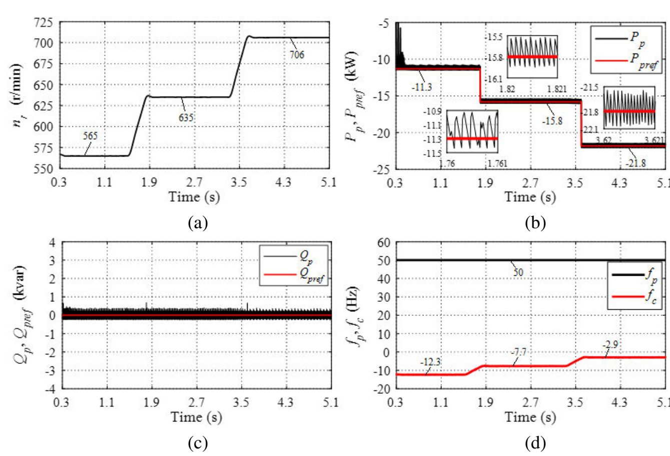

Fig. 9. Simulation results of DPC with MPPT. (a) rotor speed, (b) real power, (c) reactive power and (d) frequency.

This article has been accepted for publication in a future issue of this journal, but has not been fully edited. Content may change prior to final publication. Citation information: DOI 10.1109/TIE.2018.2811370, IEEE Transactions on Industrial Electronics

TABLE III
OPTIMUM SWITCHING VECTORS FOR THE PROPOSED DIRECT POWER CONTROL STRATEGY

Error		Sector(k)											
dP_p	dQ_p	I	II	III	IV	V	VI	VII	VIII	IX	X	XI	XII
1	1	$31'$	$31'$	$51'$	$51'$	$53'$	$53'$	$13'$	$13'$	$15'$	$15'$	$35'$	$35'$
		$46'$	$46'$	$42'$	$42'$	$62'$	$62'$	$64'$	$64'$	$24'$	$24'$	$26'$	$26'$
	0	$15'$	$35'$	$35'$	$31'$	$31'$	$51'$	$51'$	$53'$	$53'$	$13'$	$13'$	$15'$
		$24'$	$26'$	$26'$	$46'$	$46'$	$42'$	$42'$	$62'$	$62'$	$64'$	$64'$	$24'$
0	1	$51'$	$53'$	$53'$	$13'$	$13'$	$15'$	$15'$	$35'$	$35'$	$31'$	$31'$	$51'$
		$42'$	$62'$	$62'$	$64'$	$64'$	$24'$	$24'$	$26'$	$26'$	$46'$	$46'$	$42'$
	0	$13'$	$13'$	$15'$	$15'$	$35'$	$35'$	$31'$	$31'$	$31'$	$51'$	$53'$	$53'$
		$64'$	$64'$	$24'$	$24'$	$26'$	$26'$	$46'$	$46'$	$42'$	$42'$	$62'$	$62'$

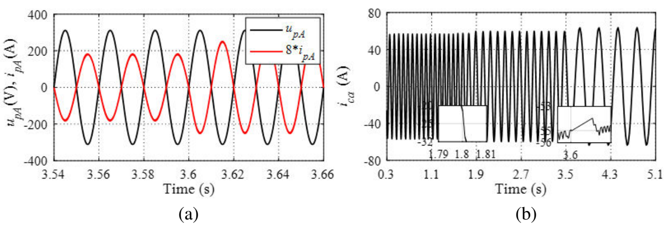

Fig. 10. Simulation traces for voltage and current in power winding and current in control winding.

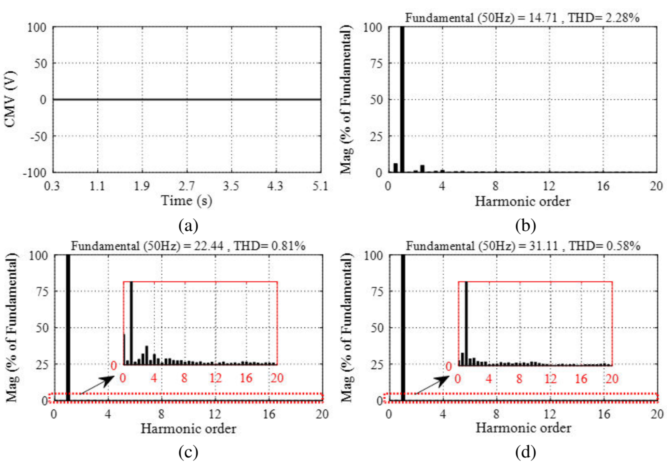

Fig. 11. Simulation results for CMV and FFT analysis of i_{pA} in different time intervals. (a) CMV. (b) FFT result in 1.01–1.05 s, THD $= 2.28\%$. (c) FFT result in 2.01–2.05 s, THD $= 0.81\%$. (d) FFT result in 4.01–4.05 s, THD $= 0.58\%$.

B. Experimental Verification and Analysis

In complience with Fig. 1 and Fig. 8, the implemented direct power control algorithm for the prominent OW-BDFRG was executed on SED-DSP28335 digital signal controller in laboratory environment as depicted in Fig. 12. A commercial induction machine (Vacon) emulating a prime mover (wind turbine) characteristics of the OW-BDFRG. The rated capacity of MSC_1, MSC_2 and GSC are rated at 15 kVA, while the IGBTs adopts Infineon. The isolated transformer is configured (380V/220V-50/60Hz-Y/D), LC filter (2.3 mH/2.5 μF-1200 VAC), power analyzer (N4L-2530), and intelligent load.

The corresponding experimental waveforms are depicted in Figs. 13–16. The OW-BDFRG rotor speed (n_r) is demonstrated in Fig. 9(a) and Fig. 13(a), and their steady state values corrolate as 565 r/min, 635 r/min and 706 r/min, respectively.

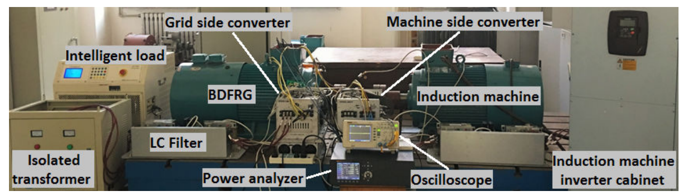

Fig. 12. The OW-BDFRG laboratory test rig for VSCF-WECS emulation.

The real power winding and its given values under the MPPT are illustrated in Fig. 9(b) and Fig. 13(b) depicted as -11.3 kW, -15.8 kW and -21.8 kW, where the tracking performance is obtained and P_p fluctuation is limited to -0.3 kW to 0.6 kW.

The Q_p trace is shown in Fig. 9(c) and Fig. 13(c), where the decoupled feature between Q_p and P_p is proven. The Q_p is virtually unaffected in an average sense, especially in high speed region after 3.5 s (Fig. 9 (c)) by a notable real power disturbances during the speed alterations. As a result, the unity power factor control (as Fig. 10 (a), the phase voltage and current of power winding is π rad out of phase, i.e., -1 for generating mode) can also be achieved by controlling $Q_p \approx 0$, which will better meet the requirement of VSCF-WECS. Furthermore, one can also observe another outstanding power decoupling control peculiarity of the proposed DPC strategy for OW-BDFRG by setting Q_p as other values, however, this is not the focus of this paper.

The power and control winding frequency, f_p (the line/grid value) and f_c, are denoted in Fig. 9(d) and Fig. 13(d). Evidently, f_p is 50 Hz, however, f_c changes to -12.3 Hz, -7.7 Hz and -2.9 Hz according to the speed plot in Fig. 9(a) and Fig. 13(a) due to the requirement in VSCF-WECS. It is worth noting that f_c is negative value which only represents its reversed phase sequence with the power windings in (3), where ω_c (also δ) is rotating clockwise in Fig. 6(b) and Fig. 14(b).

The control winding phase current waveform (i_{ca}) can be obtained as Fig. 10(b) and Fig. 14(a), where the f_c values correspond to Fig. 9(d) and Fig. 13(d) for the OW-BDFRG VSCF-WECS. As shown as the enlarged view in Fig. 10(b), one can find that the proposed DPC system has a fast dynamic performance of i_{ca} along with n_r changes for keeping f_p constant (50 Hz). Fig. 14(b) shows that the sector numbers of ψ_c changes descendingly, also the ω_c rotates clockwise, '$f_c < 0$' as Fig. 9(d) and Fig. 13(d).

The CMV of the proposed dual two-level converters are

This article has been accepted for publication in a future issue of this journal, but has not been fully edited. Content may change prior to final publication. Citation information: DOI 10.1109/TIE.2018.2811370, IEEE Transactions on Industrial Electronics

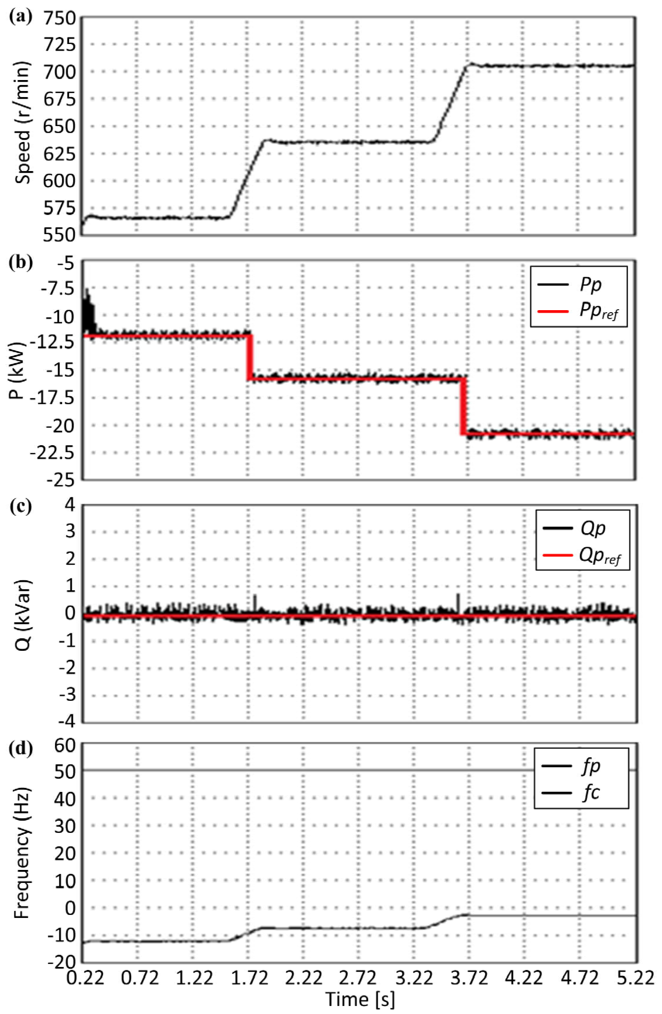

Fig. 13. Experimental results of DPC performance for speed, active power, reactive power and power winding frequency (f_p) and control winding frequency (f_c) in a limited speed range.

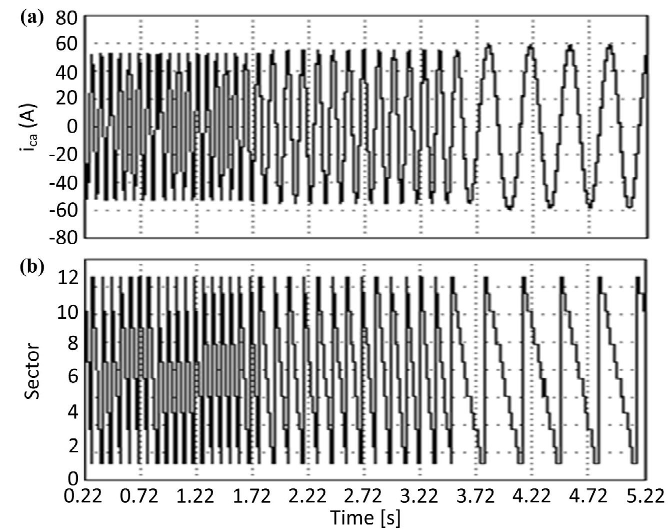

Fig. 14. Experimental traces of the DPC strategy illustrating the control a-phase current and the inferred sector number of the secondary flux.

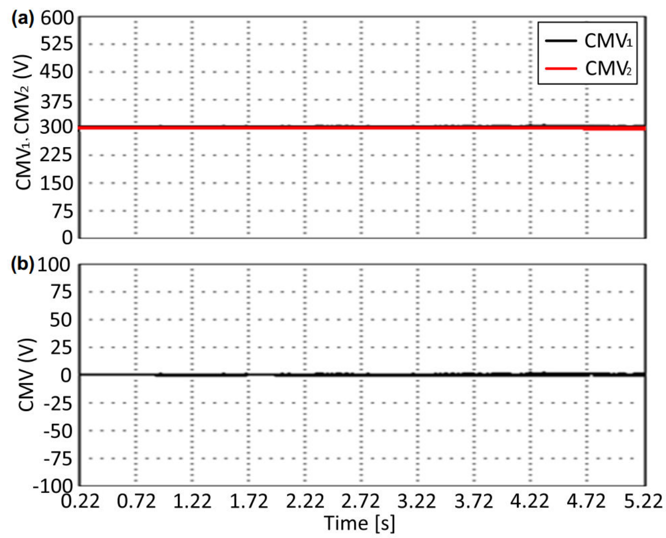

Fig. 15. Experimental waveform of the DPC strategy for common mode voltage (CMV) elimination under consideration.

illustrated as Fig. 11(a) and Fig. 15(b), where the CMV is almost kept to zero with $\mathrm{CMV}_{\mathrm{MSC}_1} \approx \mathrm{CMV}_{\mathrm{MSC}_2}$ shown in Fig. 15(a) considering (10) and Table III. Then, the common mode current and induction shaft current are eliminated/reduced, thus the service life of the OW-BDFRG will be prolonged. The power winding phase current (i_{pA}) and its total harmonic distortion (THD) during different speeds in Fig. 9(a) and Fig. 13(a) in different time intervals 1.01–1.05 s, 2.01–2.05 s and 4.01–4.05 s are given in Fig. 11(b)–(d) and Figs. 16(a)–(c), where the fundamental amplitudes of i_{pA} are approximately 14 A, 22 A and 31 A, and their THD are 2.28%, 0.81%, 0.58% and 2.42%, 0.83%, 0.59% according to the simulation results and experimental measurements, respectively.

From the above analyses, one can obtain that the proposed DPC strategy for OW-BDFRG fed by dual two-level converters with CMV elimination has many good and advantageos features for VSCF-WECS, which makes the BDFGs as a prime candidate for broader application prospect, especially for the off-shore VSCF-WECS.

V. Conclusion

In this paper a robust and machine parameter independent direct power control for the OW-BDFRG fed by dual two-level converter topology using a common DC bus with common mode voltage elimination is investigated. With the optimized synthesis scheme of the switching vectors on the machine side converter, as a result, the validity and feasibility of the proposed controller strategy are evaluated and validated through simulation and experimental test results. Compared to the traditional three-level converter systems usually adopted in the medium to large capacity converter-fed systems, the main circuit structure is simpler and easier to control. Moreover, the DC bus voltage is much lower, the redundancy of medium vectors are twice of the three-level converter and fault tolerances are much higher. In addition, the voltage levels are much better hence the smaller THD than the typical two-level converter-fed systems.

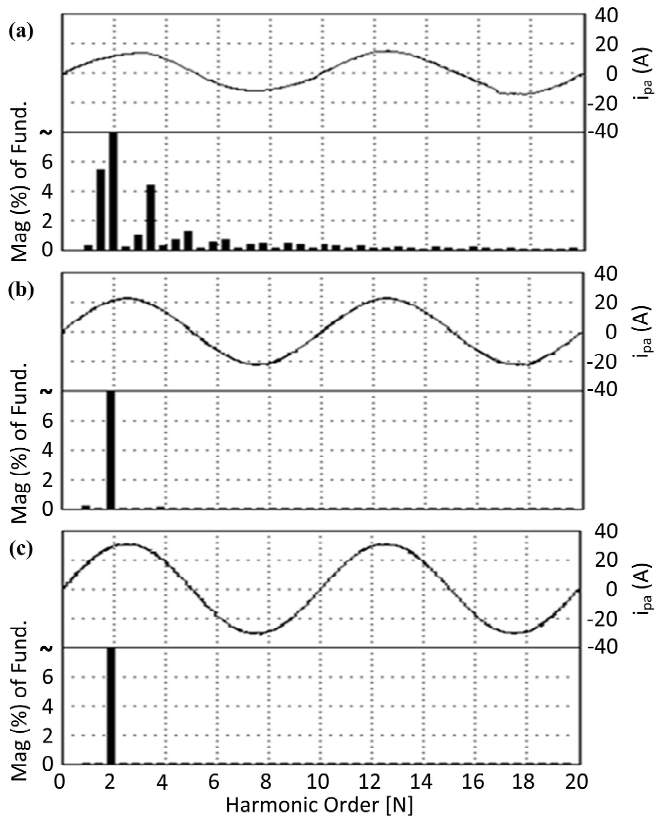

Fig. 16. Experimental results showing the power winding phase current and fundamental frequency at three different time intervals in correspondence to Fig. 13(a).

Other important features of the proposed strategy are the response and disturbance rejection aptitudes of active and reactive power controllers, coupled with the fast computation efficacy and ease of execution, which could further strengthen the controller strategy standing as a viable competitor to model-based or proportional-integral control strategies. Such advantages, besides the rotor position and speed independence formulate the basis for facilitated parameter independence DPC of VSCF-WECS. Therefore, this paper provides a good reference to further research on the relevant control strategy and also improve the performance of the large-scale wind turbines, hydro-power generators or pump-alike applications.

REFERENCES

[1] X. Wei, M. Cheng, W. Wang, P. Han, and R. Luo, "Direct voltage control of dual-stator brushless doubly fed induction generator for stand-alone wind energy conversion systems," *IEEE Trans. Magn.*, vol. 52, DOI 10.1109/TMAG.2016.2526049, no. 7, pp. 1–4, Jul. 2016.

[2] P. Han, M. Cheng, X. Wei, and Y. Jiang, "Steady-state characteristics of the dual-stator brushless doubly-fed induction generator," *IEEE Trans. Ind. Electron.*, vol. 65, DOI 10.1109/TIE.2017.2716904, no. 1, pp. 200–210, Jan. 2018.

[3] M. Jovanovic and H. Chaal, "Wind power applications of doubly-fed reluctance generators with parameter-free hysteresis control," *Energy Convers. Manage.*, vol. 134, DOI 10.1016/j.enconman.2016.10.064, pp. 399–409, Feb. 2017.

[4] A. Oraee, E. Abdi, and R. A. McMahon, "Converter rating optimization for a brushless doubly fed induction generator," *IET Renew. Power Gener.*, vol. 9, DOI 10.1049/iet-rpg.2014.0249, no. 4, pp. 360–367, Apr. 2015.

[5] X. Wang, H. Lin, and Z. Wang, "Transient control of the reactive current for the line-side converter of the brushless doubly-fed induction generator in stand-alone operation," *IEEE Trans. Power Electron.*, vol. 32, DOI 10.1109/TPEL.2016.2609461, no. 10, pp. 8193–8203, Oct. 2017.

[6] M. G. Jovanović, R. E. Betz, and J. Yu, "The use of doubly fed reluctance machines for large pumps and wind turbines," *IEEE Trans. Ind. Appl.*, vol. 38, DOI 10.1109/TIA.2002.804749, no. 6, pp. 1508–1516, Dec. 2002.

[7] R. Zhao, A. Zhang, Y. Ma, X. Wang, J. Yan, and Z. Ma, "The dynamic control of reactive power for the brushless doubly fed induction machine with indirect stator-quantities control scheme," *IEEE Trans. Power Electron.*, vol. 30, DOI 10.1109/TPEL.2014.2365675, no. 9, pp. 5046–5057, Sept. 2015.

[8] J. Njiri and D. Soffker, "State-of-the-art in wind turbine control: trends and challenges," *Renew. Sustain. Energy Rev.*, vol. 60, DOI 10.1016/j.rser.2016.01.110, pp. 377–393, Jul. 2016.

[9] S. Tohidi, H. Oraee, M. R. Zolghadri, S. Shao, and P. Tavner, "Analysis and enhancement of low-voltage ride-through capability of brushless doubly fed induction generator," *IEEE Trans. Ind. Electron.*, vol. 60, DOI 10.1109/TIE.2012.2190955, no. 3, pp. 1146–1155, Mar. 2013.

[10] S. Yu, F. Zhang, and H. Wang, "Parameter calculation and analysis of a novel wind power generator," *IEEE Trans. Magn.*, vol. 53, DOI 10.1109/TMAG.2017.2697999, no. 11, pp. 1–7, Nov. 2017.

[11] S. Jin, L. Shi, L. Zhu, W. Cao, T. Dong, and F. Zhang, "Dual two-level converters based on direct power control for open-winding brushless doubly-fed reluctance generator," *IEEE Trans. Ind. Appl.*, vol. 53, DOI 10.1109/TIA.2017.2693959, no. 4, pp. 3898–3906, Jul. -Aug. 2017.

[12] S. Ademi and M. G. Jovanović, "Vector control methods for brushless doubly fed reluctance machines," *IEEE Trans. Ind. Electron.*, vol. 62, DOI 10.1109/TIE.2014.2327564, no. 1, pp. 96–104, Jan. 2015.

[13] S. Ademi, M. G. Jovanović, and M. Hasan, "Control of brushless doubly-fed reluctance generators for wind energy conversion systems," *IEEE Trans. Energy Convers.*, vol. 30, DOI 10.1109/TEC.2014.2385472, no. 2, pp. 596–604, Jun. 2015.

[14] S. Ademi, M. G. Jovanović, H. Chaal, and W. Cao, "A new sensorless speed control scheme for doubly fed reluctance generators," *IEEE Trans. Energy Convers.*, vol. 31, DOI 10.1109/TEC.2016.2533609, no. 6, pp. 993–1001, Sept. 2016.

[15] H. Chaal and M. Jovanović, "Toward a generic torque and reactive power controller for doubly fed machines," *IEEE Trans. Power Electron.*, vol. 27, DOI 10.1109/TPEL.2011.2160731, no. 1, pp. 113–121, Jan. 2012.

[16] I. Sarasola, J. Poza, M. A. Rodriguez, and G. Abad, "Direct torque control design and experimental evaluation for the brushless doubly fed machine," *Energy Convers. Manage.*, vol. 52, DOI 10.1016/j.enconman.2010.09.018, no. 2, pp. 1226–1234, Feb. 2011.

[17] M. G. Jovanović, J. Yu, and E. Levi, "Encoderless direct torque controller for limited speed range applications of brushless doubly fed reluctance motors," *IEEE Trans. Ind. Appl.*, vol. 42, DOI 10.1109/TIA.2006.872955, no. 3, pp. 712–722, May-Jun. 2006.

[18] H. Chaal and M. Jovanović, "Practical implementation of sensorless torque and reactive power control of doubly fed machines," *IEEE Trans. Ind. Electron.*, vol. 59, DOI 10.1109/TIE.2011.2161065, no. 6, pp. 2645–2653, Jun. 2012.

[19] M. Schweizer, T. Friedli, and J. W. Kolar, "Comparative evaluation of advanced three-phase three-level inverter/converter topologies against two-level systems," *IEEE Trans. on Ind. Electron.*, vol. 60, DOI 10.1109/TIE.2012.2233698, no. 12, pp. 5515–5527, Dec. 2013.

[20] V. Somasekhar, S. Srinivas, and K. K. Kumar, "Effect of zero-vector placement in a dual-inverter fed open-end winding induction motor drive with alternate sub-hexagonal center PWM switching scheme," *IEEE Trans. Power Electron.*, vol. 23, DOI 10.1109/TPEL.2008.921170, no. 3, pp. 1584–1591, May 2008.

[21] S. Lakhimsetty, N. Surulivel, and V. T. Somasekhar, "Improvised SVPWM strategies for an enhanced performance for a four-level open-end winding induction motor drive," *IEEE Trans. Ind. Electron.*, vol. 64, DOI 10.1109/TIE.2016.2632059, no. 4, pp. 2750–2759, Apr. 2017.

[22] A. Nabae, I. Takahashi, and H. Akagi, "A new neutral-point-clamped PWM inverter," *IEEE Trans. Ind. Appl.*, vol. IA-17, DOI 10.1109/TIA.1981.4503992, no. 5, pp. 518–523, Sept. 1981.

[23] Y. Zhou and N. Heng, "Zero-sequence current suppression strategy of open-winding PMSG system with common DC bus based on zero vector redistribution," *IEEE Trans. Ind. Electron.*, vol. 62, DOI 10.1109/TIE.2014.2366715, no. 6, pp. 3399–3408, Jun. 2015.

[24] H. Zhan, Z. Q. Zhu, M. Odavic, and Y. Li, "A novel zero-sequence model-based sensorless method for open-winding PMSM

This article has been accepted for publication in a future issue of this journal, but has not been fully edited. Content may change prior to final publication. Citation information: DOI 10.1109/TIE.2018.2811370, IEEE Transactions on Industrial Electronics

with common DC bus," *IEEE Trans. Ind. Electron.*, vol. 63, DOI 10.1109/TIE.2016.2585465, no. 11, pp. 6777–6789, Nov. 2016.

[25] A. Edpuganti and A. Rathore, "Optimal pulsewidth modulation for common-mode voltage elimination scheme of medium-voltage modular multilevel converter-fed open-end stator winding induction motor drives," *IEEE Trans. Ind. Electron.*, vol. 64, DOI 10.1109/TIE.2016.2586678, no. 1, pp. 848–856, Jan. 2017.

[26] M. Cheng, P. Han, G. Buja, and M. G. Jovanović, "Emerging multiport electrical machines and systems: Past developments, current challenges and future prospects," *IEEE Trans. Ind. Electron.*, vol. PP, DOI 10.1109/TIE.2017.2777388, no. 99, Nov. 2017.

Fengge Zhang (M'17) was born in 1963. He received the B.E.E., M.S., and Ph.D. degrees from the Shenyang University of Technology, Shenyang, China, in 1984, 1990, and 2000, respectively, all in electrical engineering.

Since 1984, he has been a Teacher with the School of Electrical Engineering, Shenyang University of Technology, where he is currently a Professor. From October 2001 to July 2002, he was a Visiting Scholar at Esslingen University of Applied Sciences, Esslingen, Germany. For the last several years, he has published numerous papers in important international conference proceedings and journals on electrical machines and control systems. His research and teaching interests include electric?magnetic theory, dynamic simulation, magnetic field analysis, optimized design, computer control technology of electrical machines, and wind power generating systems. He is also active in the area of power converters for variable speed control and drive systems.

Dr. Zhang received six paper awards from Liaoning Province and four research awards from the National Machine Industry Ministry, Liaoning Province and Shenyang City, for his outstanding research accomplishments from various research projects completed in recent years. He has been confirmed as a Young Academic Skeleton by Liaoning Province and National Machine Industry Ministry. He received financial aid from the National Natural Science Foundation of China for his research project Magnetic Field Modulation Doubly-Fed Brushless AC Machine, and from Liaoning Province and others.

Liancheng Zhu was born in 1979. He received the B.S. and M.S. degree in industry electric automation, control theory and control engineering from the University of Science and Technology Anshan and University of Science and Technology Liaoning, Anshan, China, in 2002 and 2007, respectively, and the Ph.D. degree in power electronics and power transmission from the Shenyang University of Technology, Shenyang, China, in 2017.

Since 2002, he has been a Teacher with the School of Electronic and Information Engineering, University of Science and Technology. His research interests include power electronics and power transmission, special motors and their control, and wind power generators and their control. He has authored or co-authored 33 papers published in important academic journals and presented at domestic and international conferences, of 23 which were cited by SCI/EI.

Shi Jin was born in 1981. She received the B.E., M.S., and Ph.D. degrees from the Shenyang University of Technology, Shenyang, China, in 2004, 2007, and 2011, respectively, all in electrical engineering.

Since 2011, she has been a Teacher with the School of Electrical Engineering, Shenyang University of Technology. Her research and teaching interests include power electronic technology, electrical machines and their control systems, and wind power generation. She has authored or co-authored 41 papers published in important academic journals and presented at domestic and international conferences, of which 32 were cited by SCI/EI.

Dr. Jin has received financial aid from the National Natural Science Foundation of China for her research project Open-Winding Brushless Doubly-Fed Wind Power Generator With Hybrid Rotor and its Direct Power Control Strategy (Grant 51277124). She was selected as for the Baiqianwan Talents Project of Liaoning Province in 2013.

Xiaoying Su was born in 1980. She received the B.S. and M.S. degrees in power system and its automation and systems engineering from the Liaoning Technical University, Fuxin, and the University of Science and Technology, Liaoning, Anshan, China, in 2002 and 2007, respectively. She is currently in her Ph.D degree in from the School of Electrical Engineering, Institute of Electric Control Technology, Shenyang University of Technology, Shenyang, China.

Since 2002, she has been a Teacher with the School of Electronic and Information Engineering, University of Science and Technology. Her research interests include power electronics and power transmission, motors and their control, and wind power generators and their control.

Sul Ademi received the B.Eng. and Ph.D. degrees in Electrical and Electronics Engineering from Northumbria University at Newcastle, U.K., in 2011 and 2014, respectively.

Since 2017, he has been with the Warwick Manufacturing Group, University of Warwick, Coventry, U.K., where he is currently a Research Fellow. His current interests are in the areas of reluctance machine drives, validation of high-performance controllers, applications of doubly-fed motors and generators, and wind energy conversion systems.

Wenping Cao (M'05-SM'11) received the B.Eng in electrical engineering from Beijing Jiaotong University, Beijing, China, in 1991, and the Ph.D. degree in electrical machines and drives from the University of Nottingham, Nottingham, U.K., in 2004.

He is currently Chair Professor of Electrical Power Engineering and Head of Power Electronics, Machines and Power System (PEMPS) Group at Aston University, Birmingham, U.K.

Prof. Cao is presently the Chairman for the Industrial Electronics Society, IEEE UK and Ireland Section, and also a ?Royal Society Wolfson Research Merit Award? holder, U.K. He was a semi-finalist at the ?Annual MIT-CHIEF Business Plan Contest?, U.S.A., in 2015; the ?Dragon?s Den Competition Award? winner from Queen?s University Belfast, U.K., in 2014, the ?Innovator of the Year Award? winner from Newcastle University, U.K., in 2013. His research interests include fault analysis and condition monitoring of electrical machines and power electronics.